

HEALTH AND MEDICINE

Magnetolectric dissociation of Alzheimer's β -amyloid aggregates

Jinhyeong Jang and Chan Beum Park*

The abnormal self-assembly of β -amyloid ($A\beta$) peptides and their deposition in the brain is a major pathological feature of Alzheimer's disease (AD), the most prevalent chronic neurodegenerative disease affecting nearly 50 million people worldwide. Here, we report a newly discovered function of magnetolectric nanomaterials for the dissociation of highly stable $A\beta$ aggregates under low-frequency magnetic field. We synthesized magnetolectric BiFeO₃-coated CoFe₂O₄ (BCFO) nanoparticles, which emit excited charge carriers in response to low-frequency magnetic field without generating heat. We demonstrated that the magnetolectric coupling effect of BCFO nanoparticles successfully dissociates $A\beta$ aggregates via water and dissolved oxygen molecules. Our cytotoxicity evaluation confirmed the alleviating effect of magnetolectrically excited BCFO nanoparticles on $A\beta$ -associated toxicity. We found high efficacy of BCFO nanoparticles for the clearance of micro-sized $A\beta$ plaques in ex vivo brain tissues of an AD mouse model. This study shows the potential of magnetolectric materials for future AD treatment using magnetic field.

INTRODUCTION

Magnetolectric materials exhibit rigidly coupled magnetic and electric polarization (1, 2), which is the basis for their unique optical (3), mechanical (4), and thermal properties (5). According to the origin of magnetolectric coupling, two different types of magnetolectric materials exist: (i) single-phase multiferroic oxides with spin-orbit interactions and (ii) heterogeneous multiphase oxides with individual magnetostrictive and piezoelectric composites linked via interfaces (6). Because of the *d*-electrons of constituent metal ions (e.g., Fe²⁺, Fe³⁺), which are essential for magnetism (partially occupied *d*-orbitals) but reduce ferroelectric order (empty *d*-orbitals) (7), many limitations have been imposed on designing multifunctional single-phase magnetolectric materials. In contrast, heterogeneous multiphase materials are dominantly influenced by the piezo-magnetolectric effect occurring at the interfaces between two different composites. Thus, interface engineering strategies, including core-shell structure fabrication, have been used to improve magnetolectric coupling of heterogeneous multiphase materials through the donation of an additional lattice strain (8).

Bismuth ferrite (BiFeO₃, BFO) and cobalt ferrite (CoFe₂O₄, CFO) are the representative single-phase magnetolectric materials that have been widely used to construct modern electronics, such as sensors, transducers, and spintronic devices (9). Compared with their single phase structure, the heterogeneous BFO-CFO system shows a much stronger magnetolectric coupling based on their well-matching lattice structure and induced piezo-magnetolectric effect as well (10). Recently, Mushtaq *et al.* (11–13) reported that BFO-coated CFO (BCFO) can efficiently generate excited charge carriers in response to low-frequency magnetic field (e.g., below 1.1 kHz). Furthermore, the magnetic field-responsive BCFO is biocompatible with human cells [e.g., osteoblasts (12) and neuronal cells (14)] and mouse models (15), hinting at its potential for medical applications.

Here, we report magnetolectric dissociation of Alzheimer's β -amyloid ($A\beta$) aggregates and neurotoxicity mitigation by BCFO nanoparticles under a low-frequency magnetic field. Alzheimer's disease (AD) is the primary cause of age-related dementia with progressive decline in cognitive functions (e.g., attention, memory, and language), ultimately leading to complete dependency and death (16). According to the amyloid hypothesis (17), overproduction of $A\beta$ peptides and accumulation of their insoluble aggregates (e.g., $A\beta$ fibrils and plaques) in the brain is the major pathological event resulting in synaptic dysfunction and neurodegeneration. As depicted in Fig. 1, we hypothesized that magnetolectric BCFO nanoparticles dissociate neurotoxic $A\beta$ aggregates into oxidized nontoxic $A\beta$ debris under a low-frequency magnetic field.

Magnetic field allows for superior tissue penetration depth suitable for noninvasive medical treatments of the adult human brain. For example, magnetic resonance imaging (MRI) can map the entire brain of patients and diagnose the early stage of AD using a magnetic field and MRI contrast agents (e.g., gadolinium and magnetite) without any surgical procedure (18, 19). In addition, irradiation of low-frequency magnetic field on the scalp—known as “transcranial magnetic stimulation”—can alleviate depression or pain symptoms by inducing intracranial electric current that causes neuronal depolarization without any brain tissue damage (20). As such, a low-frequency magnetic field (e.g., below 1 kHz) with a nonthermal effect is medically acceptable for treating neural tissue (21), in contrast to a high-frequency magnetic field inducing a substantial amount of heat generation (22). In addition, low-frequency magnetic field has a much lower risk of causing damage to the outer tissues (e.g., scalp and skull) for the deep brain treatment in patients than other physical stimuli, including mechanical vibration (ultrasound), heat radiation (infrared light), and ionizing radiation (x-ray) (23, 24). Herein, we propose a previously unknown biomaterial platform using low-frequency magnetic field that can overcome the potential risk of the conventional approaches [e.g., sonodynamic (25, 26), photodynamic (27–29), radiodynamic (30), and magnetic hyperthermia platforms (31)]. In the current study, we unveil the potential of magnetolectric materials for low-frequency magnetic field-induced dissociation of toxic $A\beta$ aggregates, a major pathological hallmark of AD.

Copyright © 2022
The Authors, some
rights reserved;
exclusive licensee
American Association
for the Advancement
of Science. No claim to
original U.S. Government
Works. Distributed
under a Creative
Commons Attribution
NonCommercial
License 4.0 (CC BY-NC).

Department of Materials Science and Engineering, Korea Advanced Institute of Science and Technology (KAIST), 335 Science Road, Daejeon 305-701, Republic of Korea.

*Corresponding author. Email: parkcb@kaist.ac.kr

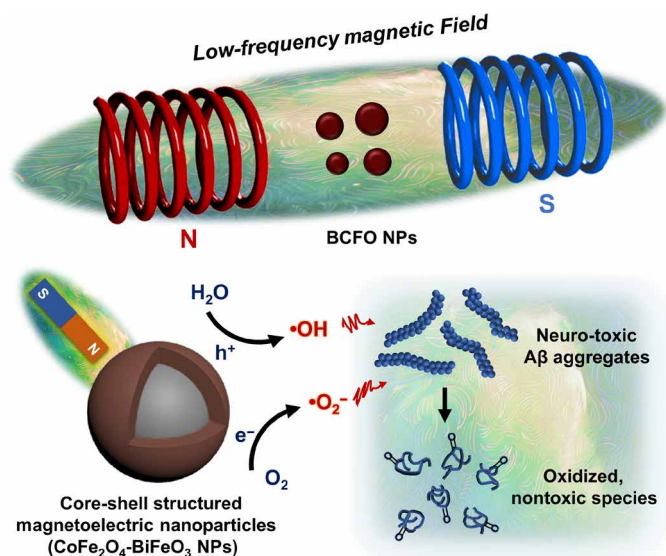


Fig. 1. Schematic illustration of magnetolectric dissociation of Alzheimer's A β aggregate structure using coreshell structured magnetolectric nanoparticles and a low-frequency magnetic field. BiFeO₃-coated CoFe₂O₄ (BCFO) nanoparticle (NP) is a magnetolectric material with strong coupled magnetic and electric ordering. Under the influence of low-frequency magnetic field, BCFO nanoparticle produces the excited charge carriers at the internal interfaces between two different magnetolectric materials. The separated charge carriers transfer from BCFO nanoparticles to water and dissolved oxygen molecules and make reactive species with a negligible amount of heat generation. Consequently, the neurotoxic A β aggregates near magnetolectrically excited BCFO nanoparticles are denatured into the oxidized nontoxic debris by the action of the reactive species.

RESULTS AND DISCUSSION

We synthesized magnetolectric BCFO nanoparticles by applying sol-gel chemistry to CFO nanoparticles (Fig. 2A). First, we prepared CFO nanoparticles through a facile hydrothermal treatment of metal ion precursors at 130°C for 15 hours according to the literature (11). The as-prepared CFO nanoparticles were black powders exhibiting a spherical morphology (Fig. 2B and fig. S1) with a size of 26.5 ± 6.2 nm ($n = 810$) (fig. S2). To make a BFO shell structure on CFO nanoparticles, we applied wet chemical coating and calcination processes to the as-prepared CFO nanoparticles with bismuth and ferric ions under different conditions. The as-synthesized BCFO nanoparticles were dark brown solids showing a CFO-like morphology (Fig. 2C and fig. S1) with a size of 33.2 ± 8.2 nm ($n = 680$) (fig. S2).

We attribute the color and size changes from CFO to BCFO nanoparticles to the BFO shell structure (approximately 3.4 nm thickness) on CFO nanoparticles. Our x-ray photoelectron spectroscopy results confirmed that BCFO nanoparticles were composed of Co²⁺, Fe³⁺, O²⁻, and Bi³⁺ (fig. S3). We investigated x-ray diffraction (XRD) patterns to examine the existence of crystalline BFO structure in BCFO nanoparticles. According to the XRD spectra (Fig. 2D), CFO nanoparticles exhibited a cubic spinel structure with the *Fd3m* space group ($a = b = c = 8.384$ Å). On the other hand, BCFO nanoparticles had not only the cubic spinel structure but also a rhombohedral perovskite structure with the *R3c* space group ($a = b = 5.5934$ Å and $c = 13.887$ Å), which is in accordance to the crystalline structure of magnetolectric BFO (32). Furthermore, our

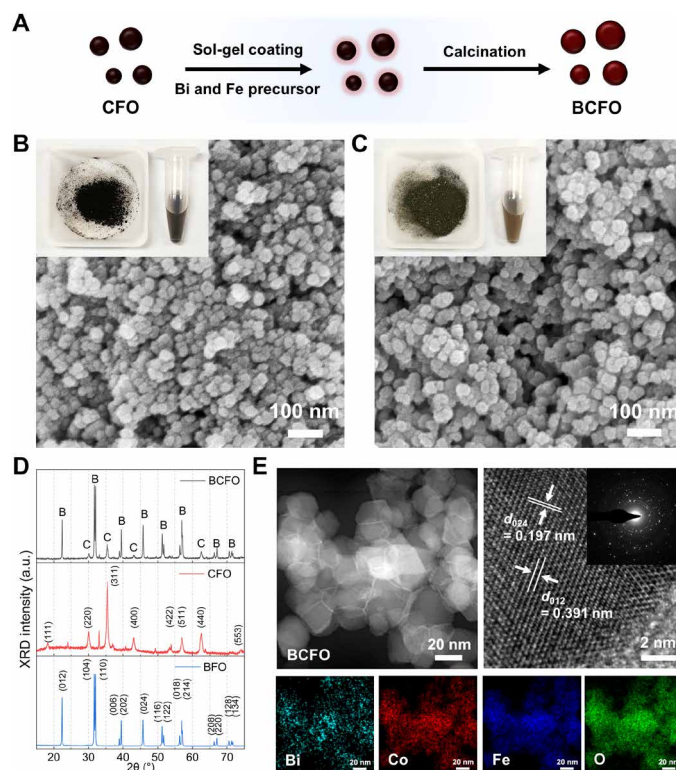


Fig. 2. Synthesis and characterization of BCFO nanoparticles. (A) Schematic illustration of the synthesis of BCFO nanoparticles using CFO nanoparticles as a core material. Scanning electron microscopy (SEM) images of (B) CFO and (C) BCFO nanoparticles with the photos of their powder and solution states (nanoparticle concentration: 2 mg ml⁻¹) (inset). (D) X-ray diffraction (XRD) analysis results of BCFO, CFO, and BFO nanoparticles. a.u., arbitrary units. (E) Transmission electron microscopy (TEM) analysis results of BCFO nanoparticles with high-angle annular dark field, high-resolution transmission electron microscopy, and energy-dispersive x-ray spectroscopy mapping results.

scanning transmission electron microscopy (TEM) images displayed the BFO shell structure on BCFO nanoparticles based on the evenly distributed constituent elements on their surface as well as its interplanar lattice spacing of 0.391 nm (Fig. 2E), corresponding to the (012) facet of the rhombohedral perovskite BFO structure (32). These results were in contrast to those of CFO nanoparticles with a different interplanar lattice spacing of 0.294 nm (fig. S4). Together, we concluded that BCFO nanoparticles had a crystalline BFO shell structure on the surface of CFO nanoparticles.

The BCFO nanoparticles produced charge carriers in response to alternating magnetic fields (Fig. 3A). To investigate BCFO's magnetic behavior, we collected magnetic hysteresis loops (from -5 to +5 T of magnetic field) at ambient conditions. As shown in Fig. 3B, CFO nanoparticles exhibited saturation magnetization (M_s) and remnant magnetization (M_r) at 113.3 and 35.4 electromagnetic units (emu) g⁻¹, respectively, indicating their room temperature (RT) ferromagnetism. BCFO nanoparticles had more enhanced ferromagnetic characteristic than CFO nanoparticles ($M_s = 123.8$ emu g⁻¹ and $M_r = 39.4$ emu g⁻¹). We attribute the increased ferromagnetism to the magnetolectric coupling of the BFO shell structure (33). The core-shell structure of BCFO nanoparticles is known to enhance the magnetic field-driven electric polarization due to the lattice strain at the interface between two different magnetolectric materials

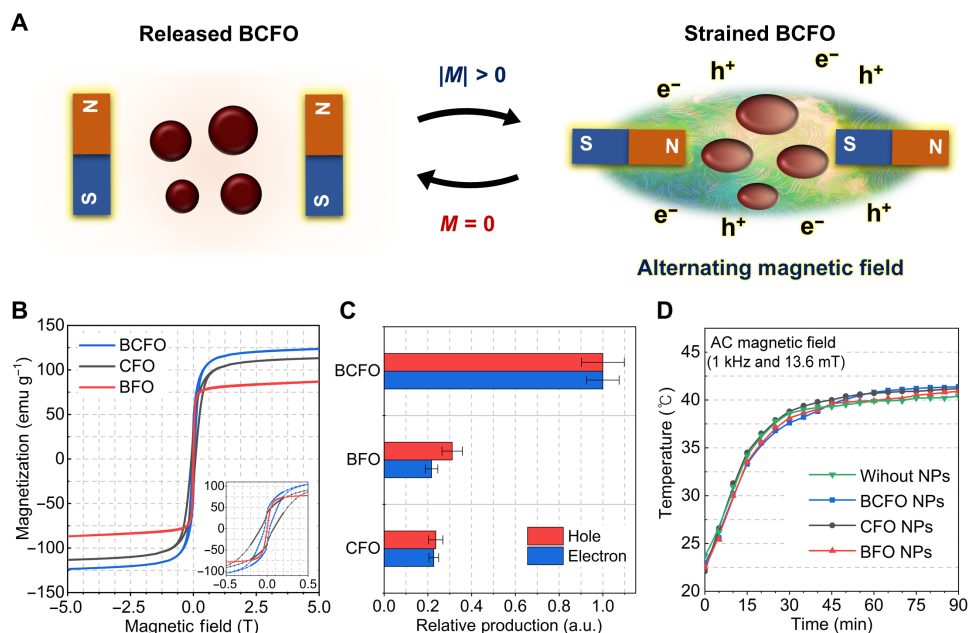


Fig. 3. Magnetic properties of BCFO nanoparticles. (A) Schematic illustration of the strain-driven excited charge carrier generation at BCFO nanoparticles in response to low-frequency magnetic field irradiation. (B) Magnetic hysteresis curves of BCFO, CFO, and BFO nanoparticles at room temperature (RT) with the range of magnetic field strength from -5 to $+5$ T. (C) Charge carrier generation and (D) system temperature change of BCFO, CFO, and BFO nanoparticle solutions under the influence of low-frequency magnetic field (1 kHz and 13.6 mT). The relative production amount of hole and electron from nanoparticles was measured by terephthalic acid (TA) and dihydroethidium (DHE) assays, respectively, after the stimulation of the low-frequency magnetic field for 1 hour. Note that the mild temperature change in condition without nanoparticles is derived from the electrical resistance effect of surrounding electromagnets and can be lowered by cooling the electromagnets (see fig. S9 for more information of the mild temperature change).

(fig. S5) (11, 34). We investigated whether the magneto-active BCFO nanoparticles can perform charge separation in response to alternating magnetic fields. According to our oscilloscopic measurements (fig. S6), BCFO nanoparticles emitted electrical pulses to the surrounding environment only when they were subjected to alternating magnetic fields.

We hypothesized that a low-frequency magnetic field (e.g., below 1 kHz) triggers catalysis at the surface of BCFO nanoparticles through the as-generated charge carriers. To examine the advent of the magnetoelectrically driven chemical reactions, we tested dihydroethidium (DHE) and terephthalic acid (TA) assays; DHE assay detects the occurrence of 2-hydroxyethidium through the electron transfer reactions and TA assay probes the generation of 2-hydroxyterephthalic acid based on the hole migration process (fig. S7) (28, 35). We found that the excited charge carriers were transferred from the surface of BCFO nanoparticles to the reactants (i.e., DHE and TA) approximately 4.2 times more than that of CFO nanoparticles under a low-frequency magnetic field (1 kHz and 13.6 mT) (Fig. 3C). The charge transfer rate of BCFO nanoparticles was proportional to the strengths (4.6, 9.2, and 13.6 mT) and frequencies (0.25, 0.5, and 1 kHz) of the alternating magnetic fields applied to the solutions (fig. S8). The BCFO nanoparticles generated a negligible amount of heat upon the irradiation of low-frequency magnetic field (Fig. 3D and fig. S9). Insignificant heat release by BCFO nanoparticles suggests that the magnetoelectric catalysis under low-frequency magnetic field (below 1 kHz) occurs regardless of the induction heating effect (also known as “magnetic hyperthermia”) of high-frequency magnetic field (e.g., 5 to 500 kHz) (22). Thus, we envisioned that the magnetoelectric catalysis triggered by

low-frequency magnetic field is suitable for the medical treatment of extremely delicate soft tissues such as the brain without any adverse thermal effect.

The highly stable β sheet-rich A β fibrils are the major proteinaceous components of A β plaques causing synaptic dysfunction and neuronal degeneration in the brain of patients with AD (36). We investigated the possibility of BCFO’s magnetoelectric coupling effect to dissociate A β fibrils under a low-frequency magnetic field (Fig. 4A). We prepared mature A β fibrils by incubating monomeric A β_{42} peptides at 37°C in an aqueous solution for 24 hours. As shown in the ex situ atomic force microscopy (AFM) images (Fig. 4B; see fig. S10 for AFM profiles), the self-assembled A β fibrils were several micrometers long with nanometer thickness, consistent with their characteristic morphologies (37). When we applied either BCFO nanoparticles (100 $\mu\text{g ml}^{-1}$) or low-frequency magnetic field (1 kHz and 13.6 mT) to an A β fibril solution (30 μM) for 6 hours, a number of elongated A β fibrils were still observed without any distinct morphological changes. In contrast, only a small amount of globular A β debris (of approximately 100 nm diameter) was found after irradiation of the low-frequency magnetic field in the presence of BCFO nanoparticles. Our scanning electron microscopy (SEM) and TEM images of the globular A β debris were consistent with the AFM images (fig. S11).

We hypothesized that the drastic morphological changes of A β fibrils were caused by the damage of the A β fibrils’ secondary structure that builds up their structural robustness. We applied thioflavin T (ThT) assay and circular dichroism (CD) analysis to evaluate the change of β sheet structure in A β fibrils. ThT is a gold standard dye for assessing the degree of amyloid aggregation because it emits

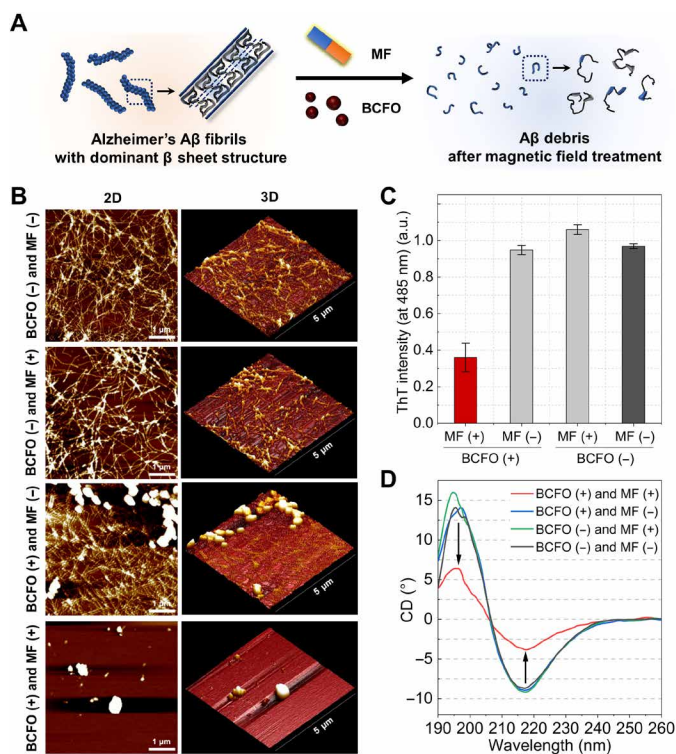


Fig. 4. Structural changes of A β fibrils. (A) Schematic illustration of magneto-electric dissociation of A β fibrils using BCFO nanoparticles and low-frequency magnetic field (MF). (B) Atomic force microscopy (AFM) images (5 μ m by 5 μ m), (C) thioflavin T (ThT) assay results, and (D) circular dichroism (CD) spectra of A β fibrils (30 μ M) after treatment of BCFO nanoparticles (100 μ g ml⁻¹) under the influence of low-frequency magnetic field (13.6 mT and 1 kHz) for 6 hours. In the AFM images, the large species in the conditions with BCFO nanoparticles represent the BCFO nanoparticle aggregates (see fig. S10 for width and height profiles of AFM images for A β fibrils and debris).

strong fluorescence upon it, binding to the β sheet structure (see fig. S12 for representative fluorescent images of ThT assay) (38). As shown in Fig. 4C and fig. S13, ThT fluorescence intensity decreased markedly from 1.00 to 0.36 after irradiation of low-frequency magnetic field in the presence of BCFO nanoparticles for 6 hours, implying the dissociation of the β sheet structure in A β fibrils. We further collected CD spectra of A β fibril solutions to spectroscopically support the ThT assay results. As shown in Fig. 4D, characteristic peak intensities of the β sheet structure (at 196 and 217 cm^{-1}) in A β fibrils were reduced by almost half when the A β fibrils were subjected to BCFO nanoparticles under low-frequency magnetic field. According to Beta Structure Selection (BeStSel) algorithm analysis results of the CD spectra, the magneto-electric treatment not only decreased β sheet structure in A β fibrils but also increased random structure (fig. S14). Note that neither BCFO nanoparticles nor low-frequency magnetic field alone could affect the native β sheet structure of A β fibrils. Furthermore, we observed that the decreased β sheet structure in the A β debris did not recover even after 72 hours of incubation at 37°C without any stimulation (fig. S15). These results imply that magneto-electrically excited BCFO nanoparticles dissociated β sheet-rich A β fibrils into thermodynamically stable, amorphous amyloid aggregates, according to the literature (39).

We attribute the results of the ThT and CD analyses to the magneto-electric coupling effect of BCFO nanoparticles. To examine the action of magneto-electric catalysis on the dissociation of A β fibrils, we used different scavengers for trapping electrons, holes, hydroxyl radicals ($\bullet\text{OH}$), and superoxide ions ($\bullet\text{O}_2^-$) (table S1). As shown in fig. S16, the dissociation of A β fibril's β sheet structure was suppressed by the depletion of not only the excited electrons and holes but also $\bullet\text{OH}$ and $\bullet\text{O}_2^-$ from the surface of BCFO nanoparticles. Note that the scavengers themselves did not change the amount of A β fibril's β sheet structures (fig. S16). Our results imply that the dissociation of A β fibrils was caused by the as-generated free radical species ($\bullet\text{OH}$ and $\bullet\text{O}_2^-$), which were generated by the charge transfer to dissolved oxygen molecules in the solution (fig. S17) (40).

According to the literature (41–43), free radical species can post-translationally modify the amino acid sequence of A β fibrils by depriving electrons from A β peptides to induce structural instability. For example, histidine (His⁶) in A β peptides can be converted to 2-oxo-histidine by the action of $\bullet\text{OH}$ and $\bullet\text{O}_2^-$ (fig. S18), and methionine (Met³⁵) also can be oxidized to methionine sulfoxide by the free radical species (fig. S19) (44). As histidine and methionine of A β peptides construct outer β strands and axial structure in A β fibrils, respectively (45–48), the oxidation of these amino acid residues can deconstruct A β fibril structure. To investigate the occurrence of oxidation on A β fibrils, we collected mass-to-charge (m/z) distributions of A β fibrils through a matrix-assisted laser desorption/ionization–time-of-flight mass spectrometry (MALDI-TOF-MS) analysis (fig. S20). In the absence of either BCFO nanoparticle or low-frequency magnetic field, A β fibrils exhibited a strong peak at m/z 4516 (A $\beta_{42} + \text{H}^+$), indicating the typical molecular weight of the pristine A β peptide. In contrast, A β fibrils after the magneto-electric treatment showed oxidation signals at m/z 4531 (A $\beta_{42} + \text{O}$). In addition, our additional MALDI-TOF-MS analysis results with laser-induced fragmentation suggested that the oxidized amino acid residue is Met³⁵, and 28.7% of Met³⁵ was converted to methionine sulfoxide after the magneto-electric treatment (fig. S21). The amount of as-produced methionine sulfoxide (28.7%) is very similar to the amount of oxidized A β peptides (30.0%) constituting A β fibrils after the magneto-electric dissociation (fig. S22). Together, our results show that magneto-electrically excited BCFO nanoparticles can dissociate β sheet structures of A β fibrils by causing the Met³⁵ oxidation of constituent A β peptides.

To examine the neural biocompatibility of BCFO nanoparticles, we tested LIVE/DEAD and Cell Counting Kit-8 (CCK-8) assays for the SH-SY5Y cell line, a common neuroblastoma model for studying neurodegenerative diseases (49). The LIVE/DEAD assay visually distinguishes live (green) and dead cells (red) using the fluorescent probes [calcein acetoxymethyl ester (calcein-AM) and ethidium homodimer-1 (EthD-1)] (50), and CCK-8 assay is a colorimetric method for assessing the mitochondrial dehydrogenase activity of live cells based on the water-soluble formazan product (26). We incubated SH-SY5Y cells with BCFO nanoparticles and applied the LIVE/DEAD assay to the cells after 1 and 7 days of cultures, respectively. As displayed in the LIVE/DEAD assay results (Fig. 5A), most SH-SY5Y cells emitted green fluorescence (live state, normal activity of intracellular esterase) even after 7 days of culture. In addition, the live cell confluence (i.e., the percentage of green color area in the captured image) was increased from 8.9% (at day 1) to 58.7% (at day 7) in the presence of BCFO nanoparticles (fig. S23), corresponding to the doubling time (approximately 2 days) of SH-SY5Y cells in the

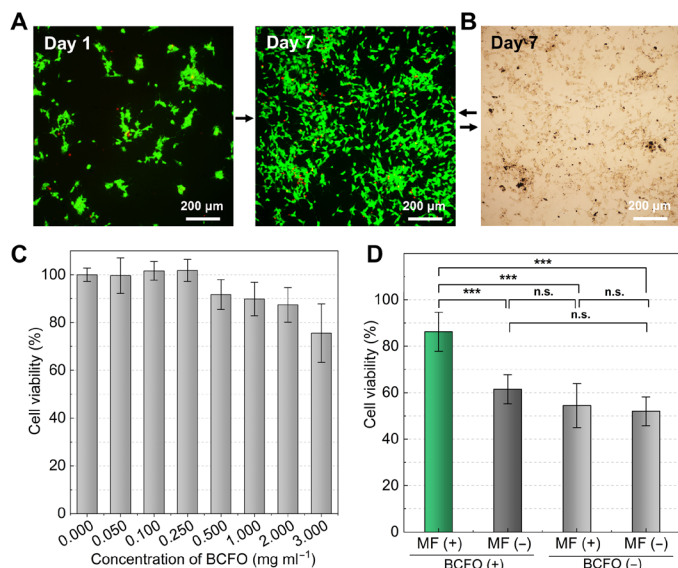


Fig. 5. In vitro evaluation results with SH-SY5Y cell line. (A) LIVE/DEAD assay results at day 1 and day 7. (B) Bright-field image at day 7. The black dots in the bright-field image represent BCFO nanoparticles. Note that the LIVE/DEAD assay and bright-field images at day 7 were captured at the same spot. (C) Cell viability with different concentrations (from 0 to 3 mg ml⁻¹) of BCFO nanoparticles. (D) Alleviating effect of BCFO nanoparticles on A β neurotoxicity under irradiation of low-frequency magnetic field (13.6 mT and 1 kHz) for 6 hours. All values were statistically analyzed by means of one-way analysis of variance (ANOVA) ($n = 4$) (***) $P < 0.001$; n.s., not significant).

healthy state (see fig. S24 for LIVE/DEAD assay with control conditions) (51). Bright-field images demonstrated BCFO nanoparticles as black dots (Fig. 5B and fig. S25) that made contact with the intact neurite outgrowths of SH-SY5Y cells (fig. S26). The neural biocompatibility of BCFO nanoparticles was also observed in differentiated SH-SY5Y cells with their long neurite outgrowths (fig. S27). In addition, CCK-8 assay results exhibited more than 90% viability of SH-SY5Y cells at up to 500 $\mu\text{g ml}^{-1}$ of BCFO nanoparticles (see Fig. 5C and fig. S28 for differentiated SH-SY5Y cells) and the negligible cytotoxic effect of BCFO nanoparticles upon the irradiation of low-frequency magnetic field as well (fig. S29). These biochemical assay results imply that the magnetoelectric treatment did not cause significant damage to the function of cellular proteins, such as intracellular esterase and mitochondrial dehydrogenase (fig. S30). Collectively, our LIVE/DEAD and CCK-8 assay results suggest neural biocompatibility of magnetoelectric BCFO nanoparticles.

We hypothesized that BCFO nanoparticles may mitigate the neurotoxicity of A β aggregates. To investigate the alleviating effect of BCFO nanoparticles, we applied CCK-8 assay to SH-SY5Y cells (Fig. 5D). When we incubated SH-SY5Y cells with mature A β fibrils (20 μM), cell viability was reduced to 53.2%. The similar low viability was shown when the A β fibrils were added into the cell culture plate after treatment of either BCFO nanoparticles (100 $\mu\text{g ml}^{-1}$) or a low-frequency magnetic field (1 kHz and 13.6 mT). On the other hand, we observed a significant recovery of the cell viability up to 85.0% after incubation with A β fibrils that were dissociated by magnetoelectrically excited BCFO nanoparticles. We attribute this result to the disassembly of the A β fibril structure. According to the literature (52, 53), accumulation of insoluble A β fibrils on the

neuronal plasma membrane induces action potential desynchronization and membrane permeation, which may trigger pathological downstream consequences including mitochondrial dysfunction and neuronal apoptosis. Our results suggest that BCFO nanoparticles and a low-frequency magnetic field may have the potential to treat not only A β fibrils but also neurotoxic A β plaques in AD brain tissue.

A β plaques are the highest-order, micrometer-sized aggregates formed by complex assembly processes between A β fibrils and biological components (e.g., lipids, protein, and metal ions) in the extracellular space of brain tissue (37). To explore A β plaque clearance efficacy of magnetoelectrically excited BCFO nanoparticles, we used ex vivo brain slices of a transgenic AD mouse model (5xFAD, 4 months of age). We applied BCFO nanoparticles (100 $\mu\text{g ml}^{-1}$) and a low-frequency magnetic field (13.6 mT and 1 kHz) to ex vivo brain slices for 6 hours (Fig. 6A; see fig. S31 for experimental setup). To highlight A β plaques, we stained the treated brain slices using thioflavin S (ThS), a fluorescent probe for labeling β sheet-dominant, neurotoxic A β plaques (54). As displayed in Fig. 6B, the cerebral cortex region of the brain slice before any treatment was covered with a significant amount of A β plaques with a density of 133.1 mm^{-2} . The brain slices after treatment of either BCFO nanoparticles or low-frequency magnetic field also exhibited a similar distribution of A β plaques to the nontreated brain slice (fig. S32). However, we found that the density of A β plaques in the cerebral cortex region drastically decreased from 133.1 to 26.4 mm^{-2} after adopting magnetoelectrically excited BCFO nanoparticles (Fig. 6C). Our immunohistochemistry analysis results also displayed the A β clearance efficacy of magnetoelectrically excited BCFO nanoparticles to ex vivo brain slices of AD mouse model (fig. S33). Furthermore, we observed that the magnetoelectrically treated brain slices did not show significant changes in their morphology and neuron distribution as well according to the Nissl staining results (fig. S34). The results show that the magnetoelectrically excited BCFO nanoparticles, which are capable of dissociating nanometer-thick A β fibrils, can also be used to clear micrometer-sized A β plaques, the major pathological hallmark of AD.

Accumulation of A β plaques in the brain of AD animal models and patients begins in the neocortex and gradually extends to the deep brain regions (e.g., hippocampus, basal ganglia, and pons) (17, 55). However, “noninvasive” treatment of the deep brain regions is limited due to the thickness of the surrounding tissue (56). Magnetic field can pass through the deep brain regions with negligible scattering and absorption losses. Our results demonstrated that relatively weak magnetic field (strength of several mT) compared to MRI scanners (strength of several tesla) can eliminate A β aggregates from the brain tissue by stimulating BCFO nanoparticles. Nevertheless, magnetoelectrically excited BCFO nanoparticles are able to induce not only dissociation of self-assembled A β aggregates but also slight secondary structure changes of single plasma proteins such as bovine serum albumin and lysozyme (fig. S35). It implies that the introduction of A β -targeting motifs into BCFO nanoparticles is necessary to prevent an unexpected adverse effect. We expect that targeted delivery of BCFO nanoparticles in the A β -accumulated specific brain regions may be achieved by coating the nanoparticle with different motifs, such as LK7 and H102 peptides (57, 58). Our spectroscopic analysis result demonstrates that BCFO nanoparticles are capable of surface functionalization for conjugating the motifs (fig. S36). To test the clinical feasibility of the magnetoelectric

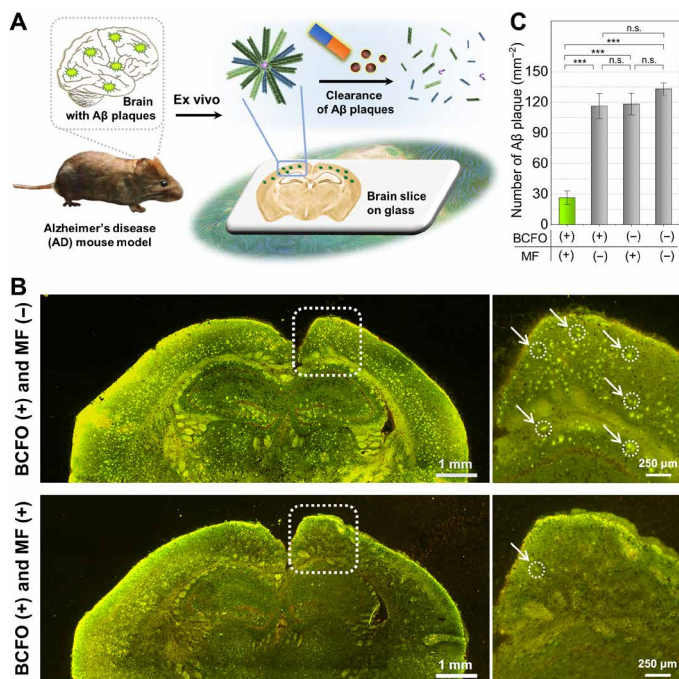


Fig. 6. Ex vivo evaluation results with the brain slices of the 5xFAD AD mouse model. (A) Schematic illustration of the disassembly of A β plaques in the brain slices by the use of BCFO nanoparticles and low-frequency magnetic field. (B) Representative microscope images and (C) A β plaque densities of the brain slices in the zoomed area after the treatment of BCFO nanoparticles ($100 \mu\text{g ml}^{-1}$) and low-frequency magnetic field (1 kHz and 13.6 mT) for 6 hours (see fig. S20 for brain slice images of the other two conditions). White dotted boxes in the entire brain slice images (left) represent the zoomed area of the brain slice (right). White dotted circles in the zoomed area (right) indicate the representative A β plaques. All values in A β plaque densities were statistically analyzed by means of one-way ANOVA ($n = 3$) (***) ($p < 0.001$).

platform in the future, we plan to conduct in vivo studies using AD mouse models for the recovery of their cognitive and behavior functions.

We report BCFO nanoparticle's newly discovered function to dissociate A β peptide aggregates under a low-frequency magnetic field. We synthesized piezo-magnetolectric BCFO nanoparticles having a core-shell structure based on two different magnetolectric materials. The BCFO nanoparticles triggered magnetolectric catalysis under a low-frequency magnetic field by transferring excited charge carriers to the surrounding environment with negligible heat generation. Magnetolectrically excited BCFO nanoparticles converted neurotoxic A β fibrils to nontoxic amorphous globular debris by oxidizing the primary structure of the constituent A β peptides and subsequently destabilizing the β sheet secondary structure of self-assembled A β fibrils. We demonstrated the clearance capability of magnetolectrically excited BCFO nanoparticles for A β fibril-dominant, micrometer-sized A β plaques that were accumulated in ex vivo brain slices of an AD mouse model. Our analysis showed that approximately 80% of A β plaques were removed without any macroscopic tissue damages after applying the magnetolectric treatment to the brain slices. This proof-of-concept study unveils the hidden function of magnetolectric nanoparticles for future treatment of AD using low-frequency magnetic field.

MATERIALS AND METHODS

Chemicals

Alzheimer's A β (1–42; human) peptide was obtained from AnaSpec (Fremont, CA, USA). Dulbecco's modified Eagle's medium (DMEM), fetal bovine serum (FBS), and antibiotic-antimycotic (AA) were purchased from Gibco (Carlsbad, CA, USA). The LIVE/DEAD assay kit was purchased from Invitrogen (Carlsbad, CA, USA). CCK-8 assay reagent was acquired from Dojindo Corp. (Japan). Antibody for immunohistochemistry was bought from Abcam (Cambridge, UK). All of the other chemicals were purchased from Sigma-Aldrich Chemical Co. (St. Louis, MO, USA).

Synthesis of CFO nanoparticles

CFO and BCFO nanoparticles were synthesized by following the literature (11, 59) and modifying minor steps. To prepare CFO nanoparticles, iron(III) chloride hexahydrate (0.995 g) and cobalt(II) chloride (0.239 g) were dissolved in aqueous solution (35 ml) containing hexadecyltrimethylammonium bromide (2.041 g) under vigorous stirring. Next, sodium hydroxide solution (6 M) was added to the mixture dropwise to adjust pH 11.0 under continuous stirring. After additional ultrasound stimulation for 30 min, the hydrothermal treatment was applied to the mixture at 180°C for 24 hours with a 50-ml Teflon-lined stainless steel autoclave. The resulting black-colored precipitates were washed with deionized (DI) water and ethanol several times after cooling down to RT. Afterward, the precipitates were collected by vacuum filtration with a 0.2- μm nylon membrane (Whatman, UK).

Synthesis of BCFO nanoparticles

To synthesize BCFO nanoparticles, the sol-gel treatment was applied to the as-prepared CFO nanoparticles. Briefly, fully dried CFO nanoparticles (50 mg) were dispersed into ethylene glycol solution (30 ml) containing bismuth(III) nitrate pentahydrate (0.160 g) and iron(III) nitrate nonahydrate (0.121 g). After 2 hours of sonication, the sol-state mixture was moved to a vacuum oven and was dried at 80°C for 24 hours. Next, the resulting gel-state mixture was preheated at 400°C for 30 min to eliminate organic compounds and successively calcined at 500°C for 90 min. The resulting BCFO nanoparticles were washed several times with DI water and ethanol on the nylon membrane and collected by a neodymium permanent magnet after ultrasound treatment.

Characterization of CFO and BCFO nanoparticles

Morphologies of CFO and BCFO nanoparticles were analyzed by SEM (S-4800, Hitachi, Japan) at 10 kV and TEM (Talos F200X, FEI Company, USA) at 200 kV. Crystallinity of nanoparticles was examined by an x-ray diffractometer (SmartLab, Rigaku Co., Japan) with Cu K α radiation ($\lambda = 1.5418 \text{ \AA}$). Chemical states of nanoparticles were obtained by an x-ray photoelectron spectrometer (Sigma Probe, Thermo Scientific, USA) with C 1s calibration to 284.6 eV. Magnetic properties of nanoparticles were analyzed by a superconducting quantum interference device-vibrating sample magnetometer (SQUID-VSM) (MPM3, Quantum Design, UK). Relative amount of as-generated holes and electrons from nanoparticles was evaluated by TA assay (3 mM) ($\lambda_{\text{ex}} = 310 \text{ nm}$ and $\lambda_{\text{em}} = 430 \text{ nm}$) and DHE assay (20 μM) ($\lambda_{\text{ex}} = 510 \text{ nm}$ and $\lambda_{\text{em}} = 590 \text{ nm}$), respectively, using a spectrofluorometer (JASCO FP6500). The magnetic field reactivity of nanoparticles was recorded by an oscilloscope (DSOX3012T, Keysight, CA, USA) under the effect of an electromagnet operated by a waveform generator (33512B, Keysight, CA, USA).

Low-frequency magnetic field stimulation

Experimental setup for magnetic field stimulation was prepared with electromagnets, which are operated by external electrical bias generated from two waveform generators (33512B, Keysight, CA, USA). Strength of applied alternating magnetic field was measured by a gaussmeter (GM07, Hirst, UK). To evaluate the magnetoelectric catalysis of nanoparticles, aqueous solution (400 μl) containing nanoparticles was subjected to alternating magnetic field under constant agitation.

Preparation and characterization of A β fibrils

Preparation of A β fibril solution (40 μM) was carried out with a biocompatible Hepes buffer (pH 7.4) following previous studies (26, 28). Morphologies of A β fibrils were recorded by an AFM instrument (NNOVA-LABRAM HR800, Horiba, Japan) (with an area of 5 μm by 5 μm and a line number of 512), SEM (S-4800, Hitachi, Japan) at 10 kV, and TEM (Talos F200X, FEI Company, USA) at 200 kV. To prepare AFM samples, A β fibril solution (10 μl) was dropped onto an AFM mica and dipped into DI water to remove excess amount of A β fibrils on the surface of mica after allowing A β fibril solution for 30 min. AFM profile analysis was performed on three independent A β fibrils. To collect SEM images, A β fibril solutions (50 μl) were coated on a gold-coated silicon wafer (1 cm by 1 cm) for 30 min before washing three times with DI water. To gather TEM images, A β fibril solutions (5 μl) were incubated on a TEM grid for 1 min, and a centrifuged lead citrate solution was applied to the grid to stain A β fibrils for 5 min before washing the grid with DI water. Protein secondary structure of A β fibrils was analyzed by ThT assay and CD spectroscopy. ThT assay results were collected through a spectrofluorometer (JASCO FP6500) by recording the fluorescence intensity ($\lambda_{\text{ex}} = 440 \text{ nm}$ and $\lambda_{\text{em}} = 485 \text{ nm}$) of mixture solution, containing ThT solution (480 μl of 20 μM) and A β solution (20 μl of 30 μM). ThT fluorescence intensity at time zero for each condition was set up as 1.0 to compare the relative amount of change in the ThT fluorescence intensity. CD spectra of A β solutions (30 μM) were acquired through a CD spectropolarimeter (Jasco-815-150 L, Jasco Inc., Japan) with a quartz cell (0.5-mm Pathlength, Jasco Inc., Japan) under N $_2$ atmosphere at RT. All CD spectra were averaged with three time measurements, and then Savitzky-Golay smoothing was processed. The β -structure selection (BeStSel) algorithm analysis of CD spectra was conducted based on the literature (60). Oxidative damage on A β fibrils was characterized by a MALDI-TOF-MS instrument (Autoflex III, Bruker Daltonics, Germany) in the positive-ion linear mode with the assistance of α -cyano-4-hydroxycinnamic acid matrix.

Cell culture

SH-SY5Y cell line (American Type Culture Collection, Manassas, VA, USA) was adapted for investigation of the biocompatibility and alleviating effect of BCFO nanoparticles. All SH-SY5Y cells were grown in complete growth medium (DMEM, 10% FBS, and 1% AA) for proliferation at a humidified environment with 37°C and 5% CO $_2$ and incubated in the differentiation medium (DMEM, 3% heat-inactivated FBS, 10 μM retinoic acid, and 1% AA) for neuronal differentiation for 7 days. During cell differentiation, fresh differentiation medium was supplied to the cell culture plate daily.

In vitro evaluations

Biocompatibility and the alleviating effect of BCFO nanoparticles were analyzed by LIVE/DEAD and CCK-8 assays. To accomplish

LIVE/DEAD assay, SH-SY5Y cells were spread at a density of 100,000 cells per well in a 12-well plate and allowed to adhere to the surface of the plate for 24 hours in a static state. Afterward, BCFO nanoparticle solution (0.5 mg ml $^{-1}$) was injected to the 12-well plate, and the SH-SY5Y cells were further incubated with BCFO nanoparticles for 7 days. Next, the SH-SY5Y cells were stained by the LIVE/DEAD assay reagents following the method used in the previous study (50). The fluorescence images of the LIVE/DEAD assay and the bright-field images were captured by a fluorescence microscope (Eclipse 80i, Nikon, Japan). See fig. S23 for the confluence analysis method in detail using LIVE/DEAD assay results. CCK-8 assay was conducted using a microplate reader (Victor 3, PerkinElmer Inc., USA) after incubating SH-SY5Y cells into a 96-well plate for 24 hours with different concentrations (0 to 3 mg ml $^{-1}$) of BCFO nanoparticles. To confirm the alleviating effect of BCFO nanoparticles, SH-SY5Y cells were differentiated for 7 days and further incubated with A β fibrils (20 μM) for 3 days before conducting the CCK-8 assay. All values in the CCK-8 assay were presented as the means \pm SD with statistical analysis using one-way analysis of variance (ANOVA).

Ex vivo evaluations

To conduct ex vivo evaluations, an AD mouse model (5xFAD, aged 4 months) was euthanized so that its brain may be used. The extracted brain was molded with frozen section medium (FSC 22, Leica, Germany) and sliced in 30 μm thickness using a cryostat (CM1860, Leica, Germany) under -19°C . The sliced brain was fixed on a histobond slide glass for further experiments. Afterward, the brain slices were treated with BCFO nanoparticle solution (100 $\mu\text{g ml}^{-1}$) and alternating magnetic field (13.6 mT and 1 kHz) for 6 hours. BCFO nanoparticles were uniformly distributed across the entire brain slices during the application of the magnetic field. Then, ThS solution [1 mM in phosphate-buffered saline (PBS) buffer] was applied to the brain slices to stain A β plaques for 1 hour and washed with a fresh PBS buffer for three times (28). Fluorescence images of ThS-stained brain slices were collected by a fluorescence microscope (Eclipse 80i, Nikon, Japan) equipped with a digital camera (DS-Ri2, Nikon, Japan). The large-size fluorescent images of the entire brain slices were collected by automatically reassembling multiple small-size snapshots through NIS-Elements software (Nikon, Japan). The fluorescent images were analyzed using ImageJ software (U.S. National Institutes of Health, MD, USA) following the method in our previous study (28). The density of A β plaques was presented with statistical analysis using one-way ANOVA. Immunohistochemistry analysis was conducted by the adoption of Alexa Fluor 488 anti-A β 1–42 antibody to ex vivo brain tissue of an AD mouse model for 1 hour staining after diluting 1:100 in PBS buffer. Nissl staining was demonstrated by the use of 0.1% cresyl violet solution in DI water for 15 min after dehydration processes with ethanol solutions.

SUPPLEMENTARY MATERIALS

Supplementary material for this article is available at <https://science.org/doi/10.1126/sciadv.abn1675>

[View/request a protocol for this paper from Bio-protocol.](#)

REFERENCES AND NOTES

1. S. Manipatruni, D. E. Nikonov, C.-C. Lin, T. A. Gosavi, H. Liu, B. Prasad, Y.-L. Huang, E. Bonturim, R. Ramesh, I. A. Young, Scalable energy-efficient magnetoelectric spin-orbit logic. *Nature* **565**, 35–42 (2019).
2. J. Long, M. S. Ivanov, V. A. Khomchenko, E. Mamontova, J.-M. Thibaud, J. Rouquette, M. Beaudhuin, D. Granier, R. A. S. Ferreira, L. D. Carlos, B. Donnadieu, M. S. C. Henriques,

- J. A. Paixão, Y. Guari, J. Larionova, Room temperature magnetoelectric coupling in a molecular ferroelectric ytterbium(III) complex. *Science* **367**, 671–676 (2020).
3. S. Toyoda, M. Fiebig, T.-H. Arima, Y. Tokura, N. Ogawa, Nonreciprocal second harmonic generation in a magnetoelectric material. *Sci. Adv.* **7**, eabe2793 (2021).
 4. M. Ghidini, R. Mansell, F. Maccherozzi, X. Moya, L. C. Phillips, W. Yan, D. Pesquera, C. H. W. Barnes, R. P. Cowburn, J. M. Hu, S. S. Dhesi, N. D. Mathur, Shear-strain-mediated magnetoelectric effects revealed by imaging. *Nat. Mater.* **18**, 840–845 (2019).
 5. R. Liu, L. Pan, S. Peng, L. Qin, J. Bi, J. Wu, H. Wu, Z.-G. Ye, The magnetoelectric effect in a cubic ferrimagnetic spinel LiFe_5O_8 with high coupling temperature. *J. Mater. Chem. C* **7**, 1999–2004 (2019).
 6. P. Wang, E. Zhang, D. Toledo, I. T. Smith, B. Navarrete, N. Furman, A. F. Hernandez, M. Telusma, D. McDaniel, P. Liang, S. Khizroev, Colossal magnetoelectric effect in core-shell magnetoelectric nanoparticles. *Nano Lett.* **20**, 5765–5772 (2020).
 7. N. A. Hill, Why are there so few magnetic ferroelectrics? *J. Phys. Chem. B* **104**, 6694–6709 (2000).
 8. Z. Huang, Ariando, X. R. Wang, A. Rusydi, J. Chen, H. Yang, T. Venkatesan, Interface engineering and emergent phenomena in oxide heterostructures. *Adv. Mater.* **30**, 1802439 (2018).
 9. J. F. Scott, Applications of magnetoelectrics. *J. Mater. Chem.* **22**, 4567–4574 (2012).
 10. Y. Li, Z. Wang, J. Yao, T. Yang, Z. Wang, J.-M. Hu, C. Chen, R. Sun, Z. Tian, J. Li, L.-Q. Chen, D. Viehland, Magnetoelectric quasi-(0-3) nanocomposite heterostructures. *Nat. Commun.* **6**, 6680 (2015).
 11. F. Mushtaq, X. Chen, H. Torlakcik, C. Steuer, M. Hoop, E. C. Siringil, X. Marti, G. Limburg, P. Stipp, B. J. Nelson, S. Pané, Magneto-electrically driven catalytic degradation of organics. *Adv. Mater.* **31**, 1901378 (2019).
 12. F. Mushtaq, H. Torlakcik, Q. Vallmajó-Martin, E. C. Siringil, J. Zhang, C. Röhrig, Y. Shen, Y. Yu, X.-Z. Chen, R. Müller, B. J. Nelson, S. Pané, Magneto-electric 3D scaffolds for enhanced bone cell proliferation. *Appl. Mater. Today* **16**, 290–300 (2019).
 13. F. Mushtaq, X. Chen, H. Torlakcik, B. J. Nelson, S. Pané, Enhanced catalytic degradation of organic pollutants by multi-stimuli activated multiferroic nanoarchitectures. *Nano Res.* **13**, 2183–2191 (2020).
 14. M. Dong, X. Wang, X.-Z. Chen, F. Mushtaq, S. Deng, C. Zhu, H. Torlakcik, A. Terzopoulou, X.-H. Qin, X. Xiao, J. Puigmartí-Luis, H. Choi, A. P. Pêgo, Q.-D. Shen, B. J. Nelson, S. Pané, 3D-printed soft magnetoelectric microswimmers for delivery and differentiation of neuron-like cells. *Adv. Funct. Mater.* **30**, 1910323 (2020).
 15. M. Ge, D. Xu, Z. Chen, C. Wei, Y. Zhang, C. Yang, Y. Chen, H. Lin, J. Shi, Magnetostrictive-piezoelectric-triggered nanocatalytic tumor therapy. *Nano Lett.* **21**, 6764–6772 (2021).
 16. D. S. Knopman, H. Amieva, R. C. Petersen, G. Chételat, D. M. Holtzman, B. T. Hyman, R. A. Nixon, D. T. Jones, Alzheimer disease. *Nat. Rev. Dis. Primers.* **7**, 33 (2021).
 17. D. J. Selkoe, J. Hardy, The amyloid hypothesis of Alzheimer's disease at 25 years. *EMBO Mol. Med.* **8**, 595–608 (2016).
 18. J. Doerr, M. K. Schwarz, D. Wiedermann, A. Leinhaas, A. Jakobs, F. Schloen, I. Schwarz, M. Diedenhofen, N. C. Braun, P. Koch, D. A. Peterson, U. Kubitschek, M. Hoehn, O. Brüstle, Whole-brain 3D mapping of human neural transplant innervation. *Nat. Commun.* **8**, 14162 (2017).
 19. C. Lian, M. Liu, J. Zhang, D. Shen, Hierarchical fully convolutional network for joint atrophy localization and Alzheimer's disease diagnosis using structural MRI. *IEEE Trans. Pattern Anal. Mach. Intell.* **42**, 880–893 (2020).
 20. J.-P. Lefaucheur, A. Aleman, C. Baeken, D. H. Benninger, J. Brunelin, V. Di Lazzaro, S. R. Filipović, C. Grefkes, A. Hasan, F. C. Hummel, S. K. Jääskeläinen, B. Langguth, L. Leocani, A. Londero, R. Nardone, J.-P. Nguyen, T. Nyffeler, A. J. Oliveira-Maia, A. Oliviero, F. Padberg, U. Palm, W. Paulus, E. Poulet, A. Quartarone, F. Rachid, I. Rektorová, S. Rossi, H. Sahlsten, M. Schecklmann, D. Szekely, U. Ziemann, Evidence-based guidelines on the therapeutic use of repetitive transcranial magnetic stimulation (rTMS): An update (2014–2018). *Clin. Neurophysiol.* **131**, 474–528 (2020).
 21. Y. I. Golovin, N. L. Klyachko, A. G. Majouga, M. Sokolsky, A. V. Kabanov, Theranostic multimodal potential of magnetic nanoparticles actuated by non-heating low frequency magnetic field in the new-generation nanomedicine. *J. Nanopart. Res.* **19**, 63 (2017).
 22. X. Liu, Y. Zhang, Y. Wang, W. Zhu, G. Li, X. Ma, Y. Zhang, S. Chen, S. Tiwari, K. Shi, S. Zhang, H. M. Fan, Y. X. Zhao, X.-J. Liang, Comprehensive understanding of magnetic hyperthermia for improving antitumor therapeutic efficacy. *Theranostics* **10**, 3793–3815 (2020).
 23. A. Bozkurt, B. Onaral, Safety assessment of near infrared light emitting diodes for diffuse optical measurements. *Biomed. Eng. Online* **3**, 9 (2004).
 24. D. L. Miller, N. B. Smith, M. R. Bailey, G. J. Czarnota, K. Hynynen, I. R. S. Makin; Bioeffects Committee of the American Institute of Ultrasound in Medicine, Overview of therapeutic ultrasound applications and safety considerations. *J. Med. Ultrasound* **31**, 623–634 (2012).
 25. S. Liang, X. Deng, P. Ma, Z. Cheng, J. Lin, Recent advances in nanomaterial-assisted combinational sonodynamic cancer therapy. *Adv. Mater.* **32**, 2003214 (2020).
 26. J. Jang, K. Kim, J. Yoon, C. B. Park, Piezoelectric materials for ultrasound-driven dissociation of Alzheimer's β -amyloid aggregate structure. *Biomaterials* **255**, 120165 (2020).
 27. J. Chen, T. Fan, Z. Xie, Q. Zeng, P. Xue, T. Zheng, Y. Chen, X. Luo, H. Zhang, Advances in nanomaterials for photodynamic therapy applications: Status and challenges. *Biomaterials* **237**, 119827 (2020).
 28. J. Jang, C. B. Park, Near-infrared-activated copper molybdenum sulfide nanocubes for phonon-mediated clearance of Alzheimer's β -amyloid aggregates. *ACS Appl. Mater. Interfaces* **13**, 18581–18593 (2021).
 29. H. Geng, Y.-c. Pan, R. Zhang, D. Gao, Z. Wang, B. Li, N. Li, D.-s. Guo, C. Xing, Binding to amyloid- β protein by photothermal blood-brain barrier-penetrating nanoparticles for inhibition and disaggregation of fibrillation. *Adv. Funct. Mater.* **31**, 2102953 (2021).
 30. X. Chen, J. Song, X. Chen, H. Yang, X-ray-activated nanosystems for theranostic applications. *Chem. Soc. Rev.* **48**, 3073–3101 (2019).
 31. H. Gavilán, S. K. Avugadda, T. Fernández-Cabada, N. Soni, M. Cassani, B. T. Mai, R. Chantrell, T. Pellegrino, Magnetic nanoparticles and clusters for magnetic hyperthermia: Optimizing their heat performance and developing combinatorial therapies to tackle cancer. *Chem. Soc. Rev.* **50**, 11614–11667 (2021).
 32. I.-T. Bae, A. Kovács, H. J. Zhao, J. Iñiguez, S. Yasui, T. Ichinose, H. Naganuma, Elucidation of crystal and electronic structures within highly strained BiFeO_3 by transmission electron microscopy and first-principles simulation. *Sci. Rep.* **7**, 46498 (2017).
 33. K. Javed, W. J. Li, S. S. Ali, D. W. Shi, U. Khan, S. Riaz, X. F. Han, Enhanced exchange bias and improved ferromagnetic properties in permalloy- $\text{BiFe}_{0.95}\text{Co}_{0.05}\text{O}_3$ core-shell nanostructures. *Sci. Rep.* **5**, 18203 (2015).
 34. J. Zhao, B. Chen, F. Wang, Shedding light on the role of misfit strain in controlling core-shell nanocrystals. *Adv. Mater.* **32**, 2004142 (2020).
 35. J. Zielonka, J. Vasquez-Vivar, B. Kalyanaram, Detection of 2-hydroxyethidium in cellular systems: A unique marker product of superoxide and hydroethidine. *Nat. Protoc.* **3**, 8–21 (2008).
 36. S. Chimon, M. A. Shaibat, C. R. Jones, D. C. Calero, B. Aizezi, Y. Ishii, Evidence of fibril-like β -sheet structures in a neurotoxic amyloid intermediate of Alzheimer's β -amyloid. *Nat. Struct. Mol. Biol.* **14**, 1157–1164 (2007).
 37. M. G. Iadanza, M. P. Jackson, E. W. Hewitt, N. A. Ranson, S. E. Radford, A new era for understanding amyloid structures and disease. *Nat. Rev. Mol. Cell Biol.* **19**, 755–773 (2018).
 38. F. Peccati, S. Pantaleone, V. Riffet, X. Solans-Monfort, J. Contreras-García, V. Guallar, M. Sodupe, Binding of thioflavin T and related probes to polymorphic models of amyloid- β fibrils. *J. Phys. Chem. B* **121**, 8926–8934 (2017).
 39. F. U. Hartl, M. Hayer-Hartl, Converging concepts of protein folding in vitro and in vivo. *Nat. Struct. Mol. Biol.* **16**, 574–581 (2009).
 40. Y. Nakabayashi, Y. Nosaka, The pH dependence of OH radical formation in photo-electrochemical water oxidation with rutile TiO_2 single crystals. *Phys. Chem. Chem. Phys.* **17**, 30570–30576 (2015).
 41. C. Cheignon, M. Tomas, D. Bonnefont-Rousselot, P. Faller, C. Hureau, F. Collin, Oxidative stress and the amyloid beta peptide in Alzheimer's disease. *Redox Biol.* **14**, 450–464 (2018).
 42. J. Kiselar, M. R. Chance, High-resolution hydroxyl radical protein footprinting: Biophysics tool for drug discovery. *Annu. Rev. Biophys.* **47**, 315–333 (2018).
 43. A. McKenzie-Coe, N. S. Montes, L. M. Jones, Hydroxyl radical protein footprinting: A mass spectrometry-based structural method for studying the higher order structure of proteins. *Chem. Rev.*, 10.1021/acs.chemrev.1c00432 (2021).
 44. L. Grassi, C. Cabrele, Susceptibility of protein therapeutics to spontaneous chemical modifications by oxidation, cyclization, and elimination reactions. *Amino Acids* **51**, 1409–1431 (2019).
 45. M. Schmidt, A. Rohou, K. Lasker, J. K. Yadav, C. Schiene-Fischer, M. Fändrich, N. Grigorieff, Peptide dimer structure in an $\text{A}\beta(1-42)$ fibril visualized with cryo-EM. *Proc. Natl. Acad. Sci. U.S.A.* **112**, 11858–11863 (2015).
 46. M. A. Wälti, F. Ravotti, H. Arai, C. G. Glabe, J. S. Wall, A. Böckmann, P. Güntert, B. H. Meier, R. Riek, Atomic-resolution structure of a disease-relevant $\text{A}\beta(1-42)$ amyloid fibril. *Proc. Natl. Acad. Sci. U.S.A.* **113**, E4976–E4984 (2016).
 47. M. T. Colvin, R. Silvers, Q. Z. Ni, T. V. Can, I. Sergeyev, M. Rosay, K. J. Donovan, B. Michael, J. Wall, S. Linse, R. G. Griffin, Atomic resolution structure of monomeric $\text{A}\beta(42)$ amyloid fibrils. *J. Am. Chem. Soc.* **138**, 9663–9674 (2016).
 48. L. Gremer, D. Schölzel, C. Schenk, E. Reinartz, J. Labahn, R. B. G. Ravelli, M. Tusche, C. Lopez-Iglesias, W. Hoyer, H. Heise, D. Willbold, G. F. Schröder, Fibril structure of amyloid- $\beta(1-42)$ by cryo-electron microscopy. *Science* **358**, 116–119 (2017).
 49. L. Agholme, T. Lindstrom, K. Kagedal, J. Marcusson, M. Hallbeck, An in vitro model for neuroscience: Differentiation of SH-SY5Y cells into cells with morphological and biochemical characteristics of mature neurons. *J. Alzheimers Dis.* **20**, 1069–1082 (2010).
 50. J. Jang, C. Cha, Multivalent polyaspartamide cross-linker for engineering cell-responsive hydrogels with degradation behavior and tunable physical properties. *Biomacromolecules* **19**, 691–700 (2018).
 51. C. C. Matthews, E. L. Feldman, Insulin-like growth factor I rescues SH-SY5Y human neuroblastoma cells from hyperosmotic induced programmed cell death. *J. Cell. Physiol.* **166**, 323–331 (1996).
 52. R. Minkevičienė, S. Rheims, M. B. Dobszay, M. Zilberter, J. Hartikainen, L. Fulop, B. Penke, Y. Zilberter, T. Harkany, A. Pitkanen, H. Tanila, Amyloid β -induced neuronal hyperexcitability triggers progressive epilepsy. *J. Neurosci.* **29**, 3453–3462 (2009).

53. F. R. Kurudenkandy, M. Zilberter, H. Biverstal, J. Presto, D. Honcharenko, R. Stromberg, J. Johansson, B. Winblad, A. Fisahn, Amyloid- β -induced action potential desynchronization and degradation of hippocampal gamma oscillations is prevented by interference with peptide conformation change and aggregation. *J. Neurosci.* **34**, 11416–11425 (2014).
54. B. Urbanc, L. Cruz, R. Le, J. Sanders, K. H. Ashe, K. Duff, H. E. Stanley, M. C. Irizarry, B. T. Hyman, Neurotoxic effects of thioflavin S-positive amyloid deposits in transgenic mice and Alzheimer's disease. *Proc. Natl. Acad. Sci. U.S.A.* **99**, 13990–13995 (2002).
55. D. R. Thal, J. Walter, T. C. Saido, M. Fändrich, Neuropathology and biochemistry of A β and its aggregates in Alzheimer's disease. *Acta Neuropathol.* **129**, 167–182 (2015).
56. J. K. Krauss, N. Lipsman, T. Aziz, A. Boutet, P. Brown, J. W. Chang, B. Davidson, W. M. Grill, M. I. Hariz, A. Horn, M. Schulder, A. Mammis, P. A. Tass, J. Volkmann, A. M. Lozano, Technology of deep brain stimulation: Current status and future directions. *Nat. Rev. Neurol.* **17**, 75–87 (2021).
57. C. Zhang, X. Zheng, X. Wan, X. Shao, Q. Liu, Z. Zhang, Q. Zhang, The potential use of H102 peptide-loaded dual-functional nanoparticles in the treatment of Alzheimer's disease. *J. Control. Release* **192**, 317–324 (2014).
58. N. Xiong, X.-Y. Dong, J. Zheng, F.-F. Liu, Y. Sun, Design of LVFFARK and LVFFARK-functionalized nanoparticles for inhibiting amyloid β -protein fibrillation and cytotoxicity. *ACS Appl. Mater. Interfaces* **7**, 5650–5662 (2015).
59. X. Wang, Y. Lin, X. Ding, J. Jiang, Enhanced visible-light-response photocatalytic activity of bismuth ferrite nanoparticles. *J. Alloys Compd.* **509**, 6585–6588 (2011).
60. A. Micsonai, F. Wien, L. Kernya, Y.-H. Lee, Y. Goto, M. Réfrégiers, J. Kardos, Accurate secondary structure prediction and fold recognition for circular dichroism spectroscopy. *Proc. Natl. Acad. Sci. U.S.A.* **112**, E3095–E3103 (2015).

Acknowledgments: We thank H. Kang at the Korea Basic Science Institute for the donation of the brain specimen extracted from a 5xFAD mouse model of AD. **Funding:** This work was supported by the National Research Foundation (NRF) via the Creative Research Initiative Center (grant number NRF-2015 R1A3A2066191), Republic of Korea. **Author contributions:** Conceptualization: J.J. Methodology: J.J. Investigation: J.J. Visualization: J.J. Supervision: C.B.P. Writing—original draft: J.J. Writing—review and editing: J.J. and C.B.P. **Competing interests:** The authors declare that they have no competing interests. **Data and materials availability:** All data needed to evaluate the conclusions in the paper are present in the paper and/or the Supplementary Materials.

Submitted 9 November 2021

Accepted 25 March 2022

Published 11 May 2022

10.1126/sciadv.abn1675